Department of Electrical and Computer Engineering
North South University

Senior Design Project

Design of a wideband metamaterial absorber for optical wavelength applications based on Hadamard matrix

Erik Upol Biswas	**ID # 1811317043**
Salman Meem Sahel	**ID # 1813077042**
MD. Moin Ebne Kamal	**ID # 1811877043**

Faculty Advisor

Dr. Mahdy Rahman Chowdhury

Associate Professor

ECE Department

Fall, 2021

DECLARATION

This is to certify that this Project is our original work. No part of this work has been submitted elsewhere partially or fully for the award of any other degree or diploma. Any material reproduced in this project has been properly acknowledged.

Students' name & Signature

1. ***Erik Upol Biswas***

2. ***Salman Meem Sahel***

3. ***MD. Moin Ebne Kamal***

APPROVAL

The capstone project entitled "**Design of a wideband metamaterial absorber for optical wavelength applications based on Hadamard matrix**" by **Erik Upol Biswas (ID#1811317043), Salman Meem Sahel (ID#1813077043),** and **MD. Moin Ebne Kamal (ID #1811877043)** is approved in partial fulfillment of the requirement of the Degree of Bachelor of Science in Computer Science and Engineering on January and has been accepted as satisfactory.

Supervisor's Signature

MAHDY

Dr. Mahdy Rahman Chowdhury
Associate Professor
Department of Electrical and Computer Engineering
North South University
Dhaka, Bangladesh.

Department Chair'sSignature

Dr. Rezaul Bari
Associate Professor
Department of Electrical and Computer Engineering
North South University
Dhaka, Bangladesh.

ACKNOWLEDGMENT

First of all, we wish to express our gratitude to the Almighty for giving us the strength to perform our responsibilities and complete the report.

The capstone project program is very helpful to bridge the gap between the theoretical knowledge and real life experience as part of Bachelor of Science (BSc) program. This report has been designed to have a practical experience through the theoretical understanding.

We also acknowledge our profound sense of gratitude to all the teachers who have been instrumental for providing us the technical knowledge and moral support to complete the project with full understanding.

It is imperative to show our appreciation for our honorable faculty member Dr. Mahdy Rahman Chowdhury for his undivided attention and help to achieve this milestone. Also, our gratefulness is divine to the North South University, ECE department for providing us a course such as EEE/CSE 499 in which we could really work on this project and materialize it the way we have dreamt of.

We thank our friends and family for their moral support to carve out this project and always offer their support.

We would also thank “Syeda Sarita Hassan” for providing the necessary support and advising us during the development of this project.

ABSTRACT

It can be a complex and daunting task to achieve broadband absorption, in this work we demonstrate a polarization insensitive ultrathin metamaterial (MM) absorber based on the Hadamard-matrix. Within the optical domain, the demonstrated MM absorber showcases absorption of over 91% for both transverse electric (TE) mode and transverse magnetic (TM) mode. To explore the angular dependence on absorption features of our Hadamard-matrix meta-absorber (HMMA), both TE and TM modes are used at numerous incident-angles. Finite integration technique was utilized to simulate the demonstrated MM absorber design and validated using the interference theory model to assure the simulated data. Moreover, electric and magnetic field characteristics, current distributions, and a plethora of parametric sweeps were also investigated in order to better understand the suggested HMMA absorption mechanism. Because of its wideband absorption and polarization insensitive characteristic, this MM absorber based on the Hadamard-matrix arrangement permits a variety of applications such as light detectors, optical-sensors, magnetic resonance imaging, plasmonic-sensors, and thermal imaging applications.

Table of Content

List of Figures

List of Tables

CHAPTER 1

Introduction

1.1 Introduction

Metamaterials are intentionally created materials composed of periodic sub-wavelength-sized unit-cell designs that exhibit exotic and unique features that are hard to acquire in natural materials, such as negative reflection or refraction, reversal of Doppler-effect, and Vavilov-Cerenkov radiation [1–8]. Because of these properties, many applications heretofore impossible have been assembled, such as stealth cloaks [9,10]. Many other potential applications in perfect absorption, imaging, and so on [11–19] have been explored. Landy and coworkers illustrated the first perfect MM absorber in 2008 [20], achieving absorption of 96% at 11.65 GHz for the very first time. Even more MM absorber research has been presented, with the operating band extending from microwave to invisible light because of the advantageous attributes of THz waves [21,22]. With FR4 and copper, Lee et al. [23] demonstrated the first broadband MM absorber in the GHz frequency range. Following that, in a series of research that has continued to this day, a broadband MM absorber in the optical domain was shown. Several of them are described in detail below, along with the findings of the studies, the substances utilized, and the materials' angular and polarization stability.

Hedayati et al. [24] demonstrated that a four-layer polarization-independent plasmonic MM absorber made of SiO2 and Au nanocomposite has an absorbance of over 85% between 400 and 750nm. Duan et al. [25] achieved over 80% absorption with four near-unity peaks from 575nm to 760nm using an MM absorber with an arbitrary cutting top layer and a quartz substrate with dual gold layers. Luo et al. [26] used Si and Ni-based MM absorbers and found that they absorbed over 90% of the light in the optical spectrum and over 99 percent between 500 and 560 nm. Heidari and Sedighy [27] demonstrated an Au & SiO2 sandwich and genetic algorithm (GA) based MM absorber with over 90% absorption and 40° polarization independence in both TE and TM modes. Zhou et al. [28] demonstrated a plasmonic broadband absorber with polarization independence up to 60° and 99.9% peak absorption at 498.25 nm. With a three-layered MM structure, Mahmud et al. [29] demonstrated 99.99% peak absorption and over 90% within the optical spectrum. Mahmud et al. reported another 99.99% peak absorption at 545.73 nm in [30], with over 90% absorption remaining within optical range. In [31] Hossain et al. used W and quartz to create an ultra-thin multi-band MM absorber with a broad incidence angle of up to 45°, absorption levels of over 66.66% from 374 to 750 nm, and a peak absorption of 99.92%. Zhang et al. [32] demonstrated a dual-band visible light absorber using an Au based resonator, with an absorption level of more than 40%, a broad incidence angle of up to 80°, and a peak absorbance of 99.9%. In addition, Charola et al. presented in [33] a numerical investigation of an MM absorber based on W and SiO2, which demonstrated an average absorption of over 90% between 404 and 631 nm with wide-angle stability up to 30°.

1.2 Project Details

In this paper, we aimed to investigate the Hadamard-matrix as a geometry design basis and to demonstrate it as a metasurface absorber for the optical regime. To generate wideband absorption, the Hadamard-matrix of rank eight $(2^{n=3})$ was selected after going through the matrix dimensions from 1 to 3 $(2^{n=1,2,3})$. The quantitative results show an optical absorption greater than 91% for both TE and TM modes for the entirety of the optical range, i.e. 380 to 700 nm and a 99.99% peak absorbance at 495.16 nm, an average absorption of 97.15% for the TEM mode, and with polarization-insensitive to 90° as well. Such a MM absorber is a viable candidate to be used as a solar cell, solar thermo-photovoltaics (STPV), and optical sensor as HMMA shifts its resonance wavelength when dielectric thickness is changed. Changing the dielectric in the Pyrex will also allow the HMMA to be used as a light detector.

1.3 Summary

This chapter gave us the insight of the overview of the proposed system. This chapter provided a clear picture on how this system is effective to use in as a metamaterial with desired outcomes.

CHAPTER 2

Methodology

2.1 Introduction

The architecture of the proposed MM absorber's unit cell is illustrated in Fig. 1, (a) & (b), which is a three-layered MM with tungsten [W, (optical, Palik)] as the resonator and ground pad, and silicon dioxide [SiO2, (optical, Ghosh)] as the intermediate dielectric substrate [34,35]. These provide the dispersion equation, optical characteristics, and band structure. W was selected as a metal and resonator layer despite its large intrinsic losses owing to its excellent impedance match with free space in the optical domain. W is an excellent absorber in its own right, with a low ohmic loss. Because of its excellent temperature stability (3422°), W is typically the best metal choice for MM absorbers in the optical domain. The lossless resonance features of SiO2 help in creating a good impedance match with the free-space of the optical region, with a high imaginary part across a wide range. The dielectric layer's low refractive index (Ri = 1.5) assists the structure in acquiring better absorbance with a wider bandwidth by aiding in the formation of suitable coupling capacitance and inductance with the resonator and metal layer. SiO2 also has a very high melting point (1710°), which will help the structure withstand the incredibly powerful electromagnetic waveform of the solar structure.

2.2 Technical Design

Our Encapsulating excellent near-unity absorption is strongly reliant on the physical dimensions of a structure and the resonator. In Fig. 1, (c) & (d) the resonator geometry is showcased and the formation of the structure was via the Hadamard matrix [36] of rank 2^n where '$\otimes$' is a recursive Kronecker product and is noted in the following equations.

$$H_n = H_1 \otimes H_{n-1} \tag{1}$$

Where,

$$H_1 = \begin{bmatrix} +1 & +1 \\ +1 & -1 \end{bmatrix} \tag{2}$$

Thus,

$$H_2 = \begin{bmatrix} +1 & +1 & +1 & +1 \\ +1 & -1 & +1 & -1 \\ +1 & +1 & -1 & -1 \\ +1 & -1 & -1 & +1 \end{bmatrix} \tag{3}$$

$$H_3 = \begin{bmatrix} +1 & +1 & +1 & +1 & +1 & +1 & +1 & +1 \\ +1 & -1 & +1 & -1 & +1 & -1 & +1 & -1 \\ +1 & +1 & -1 & -1 & +1 & +1 & -1 & -1 \\ +1 & -1 & -1 & +1 & +1 & -1 & -1 & +1 \\ +1 & +1 & +1 & +1 & -1 & -1 & -1 & -1 \\ +1 & -1 & +1 & -1 & -1 & +1 & -1 & +1 \\ +1 & +1 & -1 & -1 & -1 & -1 & +1 & +1 \\ +1 & -1 & -1 & +1 & -1 & +1 & +1 & -1 \end{bmatrix} \tag{4}$$

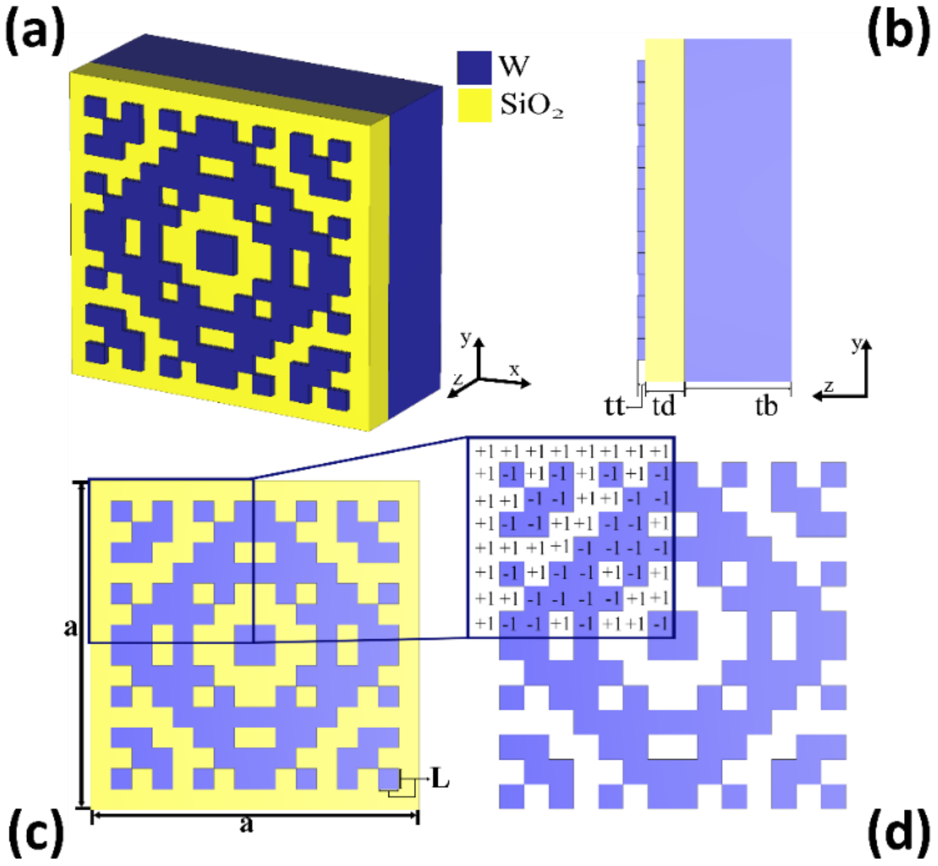

Fig. 1. Schematic of the unit cell, (a) 3-D view, (b) side view with dimensions, (c) top surface view with dimensions, and (d) top surface design relation with Hadamard matrix.

When constructing the resonator, we assumed -1 to be the position where we would use W, leaving +1 without any metal. We also made sure to test for the opposite, where +1 is the position where W was used and -1 neglected. After seeing both results, we concluded that -1 with W produced better and more desirable results. Table 1 has a complete list of the optimized parameters used. While designing the MM absorber firstly the back-layer metal thickness was made greater than the MM absorber's skin-depth, $(\delta) = \sqrt{(2\rho/2\pi f \mu_R \mu_0)}$ so as to guarantee near-zero transmission in the full optical domain. The rest of the parameters observed was optimized through various parameter sweeps. As it will be demonstrated below in Table 1, with adequate data, this design has a logical, symmetrical structure. The entire thickness of the unit cell is 216 nm, which is ultrathin. These ultrathin structures are readily adaptable to any STPV cell. From the + z-axis, the TE and TM modes are shined. Using the commercially available CST Microwave Studio (CST MWS) software, all simulations are run for a single unit cell. In the x and y axis, unit cell boundary conditions were used, but the z axis was left with open add space. A higher mesh order was employed to render the simulation results more precise. All of the studies were conducted using frequency-domain analysis based on the finite integration technique (FIT).

Table 1. The Proposed Unit Cell Design's Parameter List

Parameters	Values (nm)
a	480
tt	11
td	55
tb	150
L	30

2.3 Summary

This chapter provided the idea about the motivation towards our project which aims to make a high grade metamaterial.

CHAPTER 3

Results Analysis and Discussion

3.1 Absorbance Methodology

The Nicolson–Ross–Weir (NRW) technique is used to calculate absorbance by extracting scattering parameters (S-parameters) [37]. Because absorbance is highly reliant on impedance matching, the unit cell's impedance.

$$Z(\omega) = \sqrt{\left[\frac{\mu_r(\omega)\mu_0}{\varepsilon_r(\omega)\varepsilon_0}\right]} \tag{5}$$

The impedance characteristics, $Z_0 = \sqrt{\mu_0/\varepsilon_r} = 376.73 \approx 377\Omega$

Where,

$\mu_0 =$ Permeability of free space.

$\mu_r =$ Relative Permeability.

$\varepsilon_0 =$ Permittivity of free space.

$\varepsilon_r =$ Relative permittivity.

By adjusting the design's physical dimensions, we can achieve the condition $\left[Z(\omega) = Z_0\right]$. And because the absorption is largely dependent on wavelength, the design will offer virtually unity-absorption at that wavelength. Here, $Z(\omega) \approx Z_0$ which is quite near to the desired value; if the value can be equaled, the design can serve as a super absorber with unity absorption. Absorption is inversely proportional to reflection coefficient $R(\omega)$ and transmission coefficient $T(\omega)$, where $R(\omega)$ is the linear value of S_{11} and $T(\omega)$ is the linear value of S_{21} S-parameters respectively. Hence, the formula can be written as,

$$A(\omega) = 1 - R(\omega) - T(\omega)$$

$$= 1 - |\mathrm{S}_{11}(\omega)|^2 - |\mathrm{S}_{21}(\omega)|^2 \tag{6}$$

Meanwhile, because the ground plate thickness is greater than the skin-depth of W, $T\left(\omega\right)$ may be represented as close to zero. As a result, the final absorption formula will be as follows,

$$\begin{aligned} A(\omega) &= 1 - R(\omega) \\ &= 1 - |\mathrm{S}_{11}\left(\omega\right)|^2 \end{aligned} \tag{7}$$

Fig. 2, (a) demonstrates the absorbance, and reflectance of transverse electromagnetic (TEM), TE, and TM modes for the optical domain of 380 to 700 nm using our proposed MM absorber with optimized parameters as shown before in Table 1. As stated before, the absorption curve is obtained from (6) and (7). The proposed HMMA structure has 99.99% absorption at 495.16 nm and above 99% absorption from 448.52 to 550.94 nm, with a wide range of 102.42 nm. Its absorption starts at 92.29% at 380 nm and 91.40% at 700 nm and has an average absorption of 97.15% for the entirety of the optical spectrum.

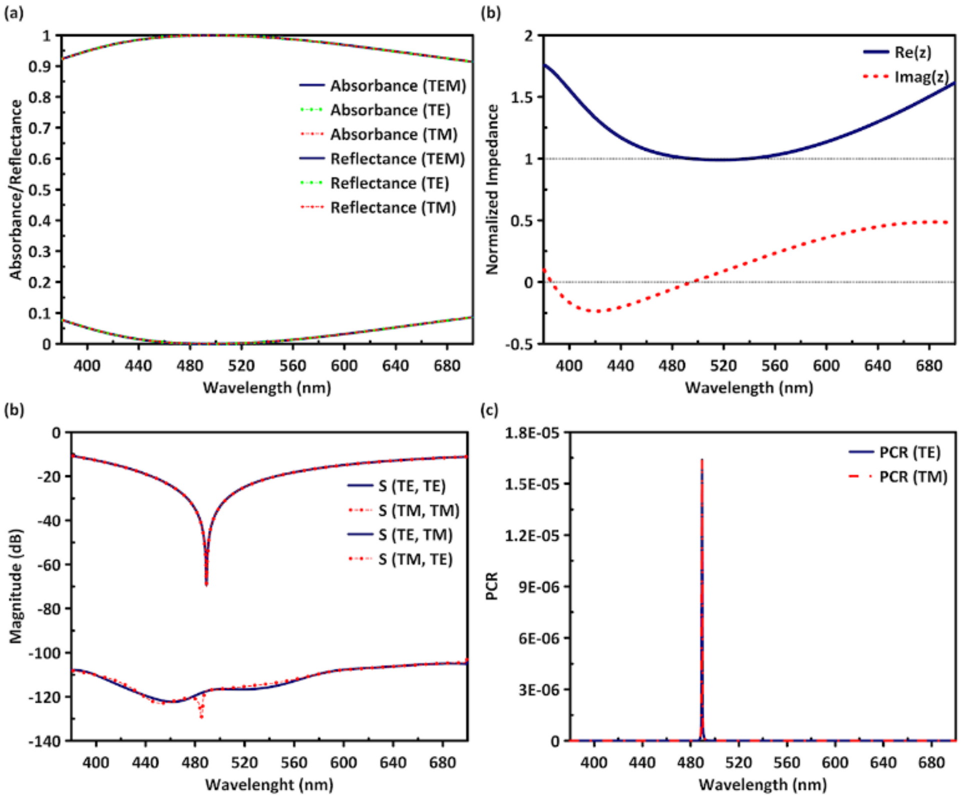

Fig. 2. Graphical representation of (a) absorbance and reflectance of TEM, TE and TM modes from wavelength 380-700 nm, (c) co-polarization and cross-polarization magnitude (dB) of the reflection coefficient for both TE and TM-polarization modes, and (d) PCR of the proposed unit cell for both TE and TM modes.

Fig. 2, (b) illustrates the normalized impedance with real and imaginary parts for TEM mode. The real portions of the normalized impedance must be near to one, meanwhile imaginary portions must stay near zero, in order to achieve a high impedance match. These two events were made possible by the unit cell architecture, which can be seen clearly in Fig. 2, (b). The decent coupling capacitive and inductance values of the metal and the resonator surface with the assistance of the dielectric is also a key factor for high absorption over the whole domain with a near-unity apex. Consequently, unless the resonator is not a symmetrical resonator with a commendable structure, it is possible that these occurrences would not be able to catch the falling waves.

The illustrations in Fig. 2, (c) & (d), shows for both TE and TM modes, co-polarization and cross-polarization and polarization conversion ratio in both magnitude (dB) scale and linear scale. These co-polarization and cross-polarization phenomenon are needed to answer whether or not the proposed HMMA is the MM absorber converting the polarization wave rather than of good absorptivity. From Fig. 2, (c), it is observed that the cross-polarization component is near zero in the linear magnitude scales, this verifies that the design did not transform the waves in the wavelength area under consideration. Co-polarization and cross-polarization can be calculated form eq. (8) & (9) as,

$$|\mathrm{S}_{11}(\omega)|^2 = |\mathrm{R}_{yy}|^2 + |\mathrm{R}_{yx}|^2 \tag{8}$$

$$|\mathrm{S}_{11}(\omega)|^2 = |\mathrm{R}_{xx}|^2 + |\mathrm{R}_{xy}|^2 \tag{9}$$

Where, R_{yx} and R_{xy} are the cross-polarization component, R_{xx} and R_{yy} are the co-polarization component. Polarization conversion ratio (PCR) can be can be calculated using the linear value of R_{xx} , R_{yy} , R_{xy} and R_{yx} with the following eq. (10) & (11).

$$PCR_{TE} = \frac{R_{yx}^2}{(\mathrm{R}_{yy}^2 + \mathrm{R}_{yx}^2)} \tag{10}$$

$$PCR_{TM} = \frac{R_{xy}^2}{(\mathrm{R}_{xx}^2 + \mathrm{R}_{xy}^2)} \tag{11}$$

3.2 Theoretical Verification

The Interference theory is employed to comprehend the absorption process of HMMA and to validate the results of our simulation. For verification, decoupled simulated data was compared to calculated data produced from the interference theory model. Fig. 3, depicts the comparison graph for difference in absorbance, the interference theory, and the decoupling model. According to interference theory [38–40], with the ground plate, total reflection $S_{11(\mathrm{Total})}$ for layer 1 can be calculated form (12) as,

$$S_{11(Total)} = |\mathrm{S}_{11}| \exp(j\theta_{11}) + \frac{|\mathrm{S}_{12}||\mathrm{S}_{21}| \exp[\mathrm{j}(\theta_{12} + \theta_{21} - 2\beta - \pi)]}{1 - |\mathrm{S}_{22}| \exp[\mathrm{j}(\theta_{22} - 2\beta - \pi)]} \tag{12}$$

Where,

$S_{11} = |S_{11}|\exp(j\theta_{11})$, $R(\omega)$ for layer one from area one to two.

$S_{11} = |S_{11}|\exp(j\theta_{11})$, $T(\omega)$ for layer one from area one to two.

$S_{11} = |S_{11}|\exp(j\theta_{11})$, $T(\omega)$ for layer one from area two to one.

$S_{11} = |S_{11}|\exp(j\theta_{11})$, $R(\omega)$ for layer one from area two to one.

Moreover, $\beta = k_0 d$ here β = complex propagation phase, k_0 = wave-number in area 2, and d = propagation distance. The symmetrical nature of the design was demonstrated in the preceding section. Hence, $[S_{12} = S_{21}]$ so we can re-write eq. (12) as,

$$S_{11(Total)} = |S_{11}|\exp(j\theta_{11}) + \frac{|S_{12}|^2 \exp[j(2\theta_{12} - 2\beta - \pi)]}{1 - |S_{22}|\exp[j(\theta_{22} - 2\beta - \pi)]} \tag{13}$$

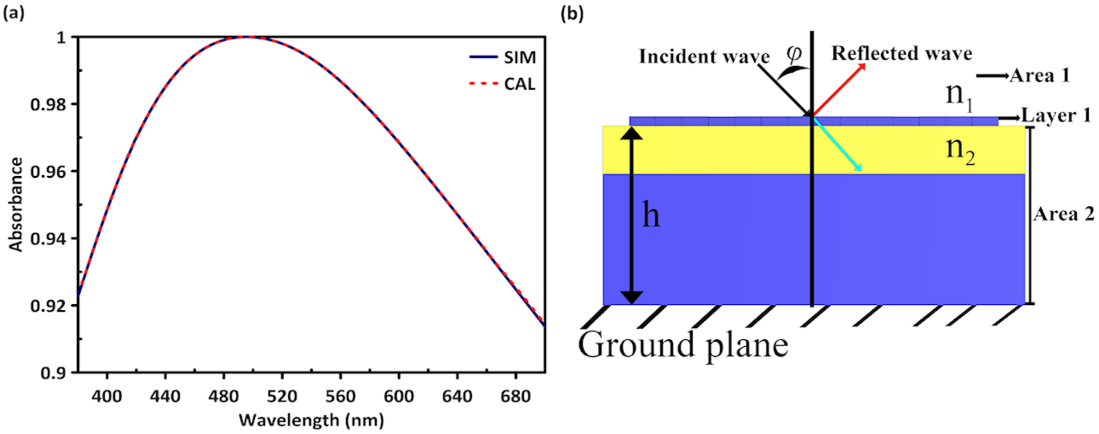

Fig. 3. (a) Comparison of the simulated absorbance with the calculated values, and (b) a schematic illustration of the interference theory structure with different incidence angles.

Ultimately, absorption may be calculated theoretically using the simple formula $A(\omega) = 1 - |S_{11(Total)}|^2$. The simulated absorbance values are quite comparable to the estimated absorbance we got from the interference theory, as shown in Fig. 3 (a). Both findings demonstrated remarkable absorption, with peak values above 99.9% for the simulated and calculated results.

3.3 Comparison of different geometry and various dielectric substrate on the unit cell

This section goes over a distinguishing feature of the proposed HMMA. When we applied a scaled configuration of the HMMA with half and further scaled it to a quarter of the original design, the HMMA showed an outstanding average absorption of 97.04% and a peak of 99.87% for the half-scaled HMMA structure, while the quarter-scaled resulted in an average absorption of 96.37% and a peak of 99.39%, as shown in Fig. 4, (a). A metamaterial unit cell may be made considerably smaller than the wavelength's free space, resulting in considerable phase variation at practical operating frequencies [41]. This is a key cause of the structure's absorption. In this case, the resonator, dielectric, and metal layers are all the same thickness. However, at half (a=240 nm) and quarter (a=120 nm) sizes, the parameter "L" is modified from 30 to 15 and 7.5 nm, respectively. Given the small size of the building, the design might be scaled down to half or a quarter of its original size.

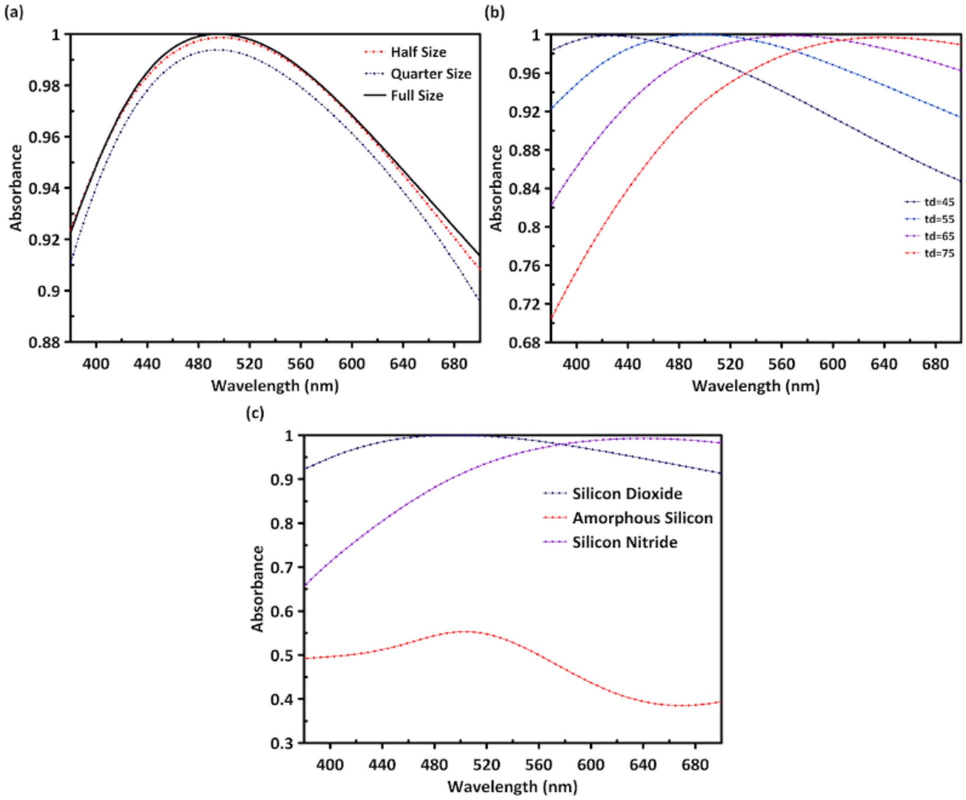

Fig. 4. (a) Absorbance comparison graph of half, quarter and full size HMMA, (b) graphical representation of a parametric sweep for the parameter “td” in TEM mode, and (c) comparison of absorbance with different types of dielectric layer in TEM mode.

In Fig, 4, (b) shows a major and important sweep of the parameter "td", which refers to the thickness of the dielectric material. A substantial change in absorbance has been detected after changing the thicknesses from 45 to 75 nm, and the resonance wavelength has also shifted significantly. The resonance wavelength changed linearly at 426.17, 495.16, 567.21, and 638.69 nm while still maintaining 99.89%, 99.99%, 99.89%, and 99.70%, respectively. When the structure is exposed to an EM wave, it generates capacitance with the metal layer and a resonator with the help of the dielectric layer. The capacitance of a structure, on the other hand, is significantly dependent on the dielectric depth and is inversely related to it. As the depth was increased, the capacitance dropped, and the responsive wavelength changed linearly from left to right. For this significant phenomenon, this structure could be employed as an optical sensor.

We also simulated our proposed HMMA structure with different dielectric materials, which is shown in Fig. 4, (c) along with SiO2, the dielectric component was replaced with three other different compounds, as in gallium arsenide, silicon nitride, and amorphous silicon, which were the new materials. In this case, we could see that SiO2 has a significantly higher average absorption than that of the other materials. The various Ri of such materials account for this type of fluctuation. Since we already know, the smaller the Ri, the greater the absorption and the wider the band. The Ri, of SiO2, Si3N4 and A-Si are 1.5, 2.0, and 4.4, respectively. That being said, because the absorption amount was linearly raised by Si3N4, it can be employed as a light detector within the visible domain. Furthermore, A-Si can be employed as half-power absorbers since they display half-absorption for nearly the entire optical domain.

3.4 Incident and polarization angle stability

As described in earlier sections, the HMMA seems to have been a wide-incidence and polarization angle stable structure in both TE and TM modes. Because of its symmetrical construction, the HMMA design is completely polarization angle insensitive from 0° to 90°, as shown in Figs. 5, (a) & (b). However, an ideal MM absorber must be constant for the incidence angle in order to be used as a solar cell, for energy harvesting, as a solar sensor or detector, or for a number of other critical applications. In Fig. 5, (c) & (d), the structure is shown from 0° to 60° with increments of 10° for various incidence angles in both TE and TM modes. The average absorbance in TE mode was more than 84.74% for all incidence angles. Because the wave's path length is exactly proportional to the angle of incidence, the greater the angle, the greater the path length. For the weaker magnetic dipolar resonance, the coupling effect of the resonator and metal reduces due to the long route. The effect affects wave confinement in the dielectric layer, resulting in reduced absorptivity.

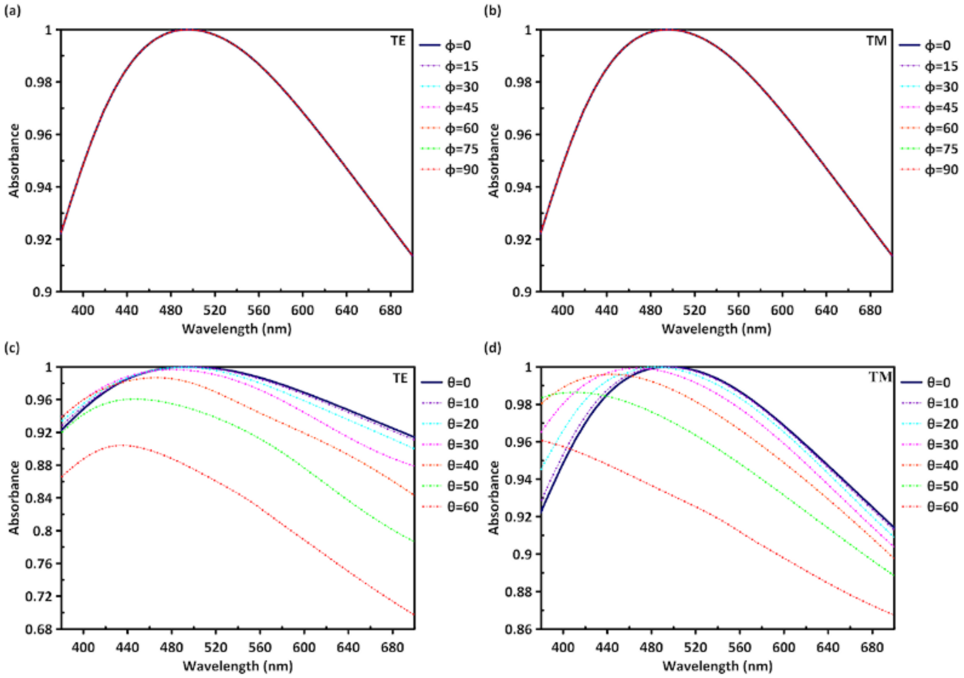

Fig. 5. Graphical representation of absorbance for different polarization angles (phi) from 0-90° (a) TE mode, (b) TM mode, and different incident angle (theta) from 0-60° for (c) TE mode, (d) TM mode.

A distinct situation arises for the TM mode shown in Fig. 5, (d), as it demonstrated superior stability with an average absorptivity that varied by more than 92.66% for an incidence angle of 60°. In the TM mode, the MMA absorptivity level does not vary as much as the incidence angle. Better stability in the TM mode is due to the bigger electric field involving the perpendicular incidence angle rather than the parallel component. Excellent coupling combined with excellent wave confinement gives this design a polarization- and incident-angle stable MM absorber, broadening its application requirements in a variety of domains.

3.5 Electric field, magnetic field and surface current distribution

The electromagnetic field and surface charge distribution influence absorption properties in both TE and TM modes. In this part, e-field, h-field, and surface current will be measured at three distinct wavelengths $\lambda = 420$, 495.16, and 690 nm, which correspond to three different absorption levels of $A(\omega) = 94.88$, 99.99, and 91.88%, respectively, as shown in Fig. (6) – (8).

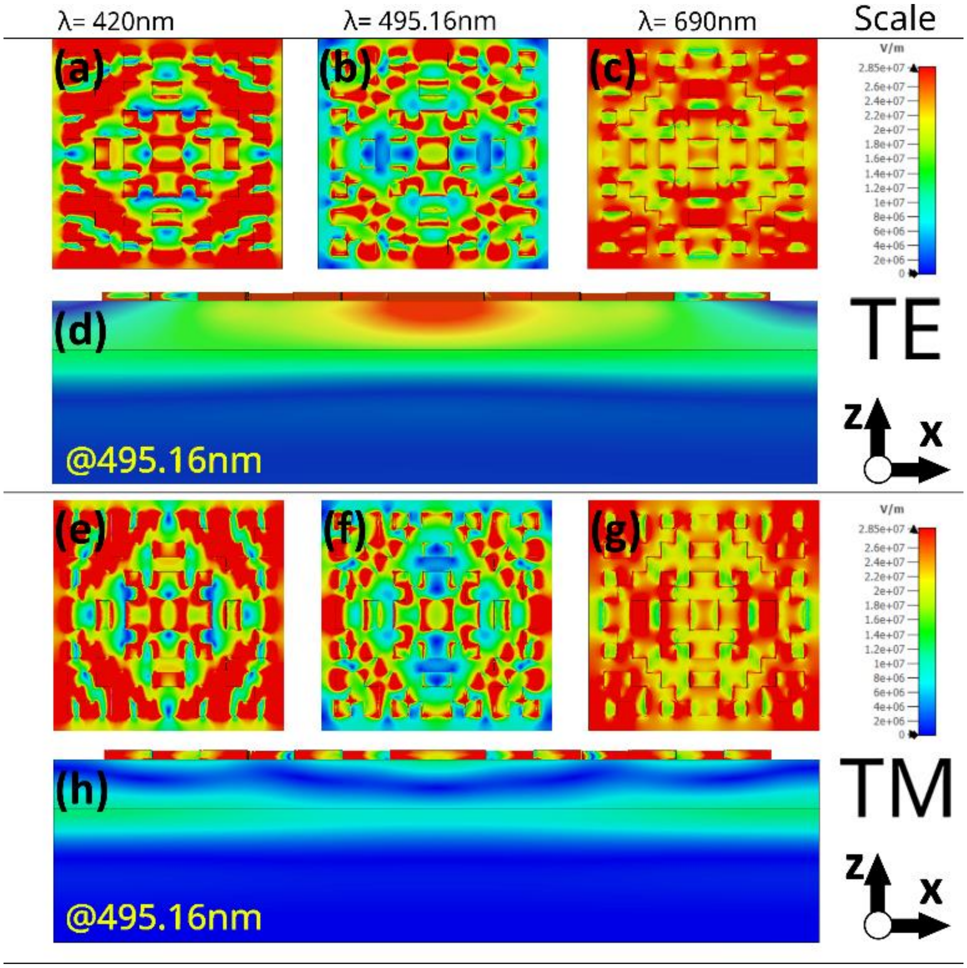

Fig. 6. Representation of electric-field distribution of the unit cell (a)-(c) for TE polarization in 420, 495.16, and 690 nm with linear color bar (Vm-1) in y-x axis, (d) cross-sectional view of the middle of the structure at 495.16nm (peak) resonance wavelength in z-x axis, (e)-(g) TM polarization in 420, 495.16, 690 nm with linear color bar (Vm-1) y-x axis, (h) cross-sectional view of the middle of the structure at 495.16nm (peak) resonance wavelength in z-x axis.

Fig. 6, shows a strong E-field for both TE and TM modes at the three previously mentioned wavelengths. As previously said, this is one of the most important causes of high absorption. The dielectric substance SiO2, which energizes the electric resonant dipolar moment, is shown to considerably restrict the E-field in Fig. 6, (d) & (h) for both TE and TM. Such high E-field regions are most often seen at the interfaces of the metal resonator or dielectric material that characterized the developing surface plasmon effect shown in Figs. 6, (a)-(c), and (e)-(g). These surface plasmons combined to produce a perfectly resonant dipole, magnifying the concentrated E-field [42,43]. As a consequence of the greater surface plasmons at the interfaces, paired with the strong optical properties of W, the MM absorber exhibited high absorption at such wavelengths. Fig. 7, depicts the H-field for both the TE and TM modes, as well as the E-field with three different wavelengths. Our suggested HMMA design exhibited a very excellent H-field distribution, transforming it into a highly efficient polarization-independent MM absorber throughout the whole optical domain. As shown in Fig. 7, its H-field is firmly centered on the metal resonator and significantly constrained by the dielectric material. As demonstrated in Fig. 7, (b) & (f), the H-field is exceptionally strong in both TE and TM modes at the maximal absorption stage of = 495.16 nm. A cross-sectional view at = 495.16 nm demonstrates that the H-field level is high near the core of the HMMA. As the polarization flips from TE to TM modes, the H-field changes solely in one direction. Anti-parallel current density from the metal layer to the metal resonator forms a loop. The artificial magnetic dipolar moment rises due to the current density, which is highly integrated into the H-field [44,45]. As a consequence, the design excites the H-field, provides a very strong magnetic resonant dipole, and produces good absorption over the whole optical domain. Another notable phenomenon, corroborated by Figs. 7, (d) & (h) is that the thickness of the back-plate metal completely prevents TE, TM, or TEM mode transmission. In Fig. 8, three distinct wavelengths were used to represent the surface charge distribution for both the TE and TM modes to better link the fields, much as in the E-field or H-field.

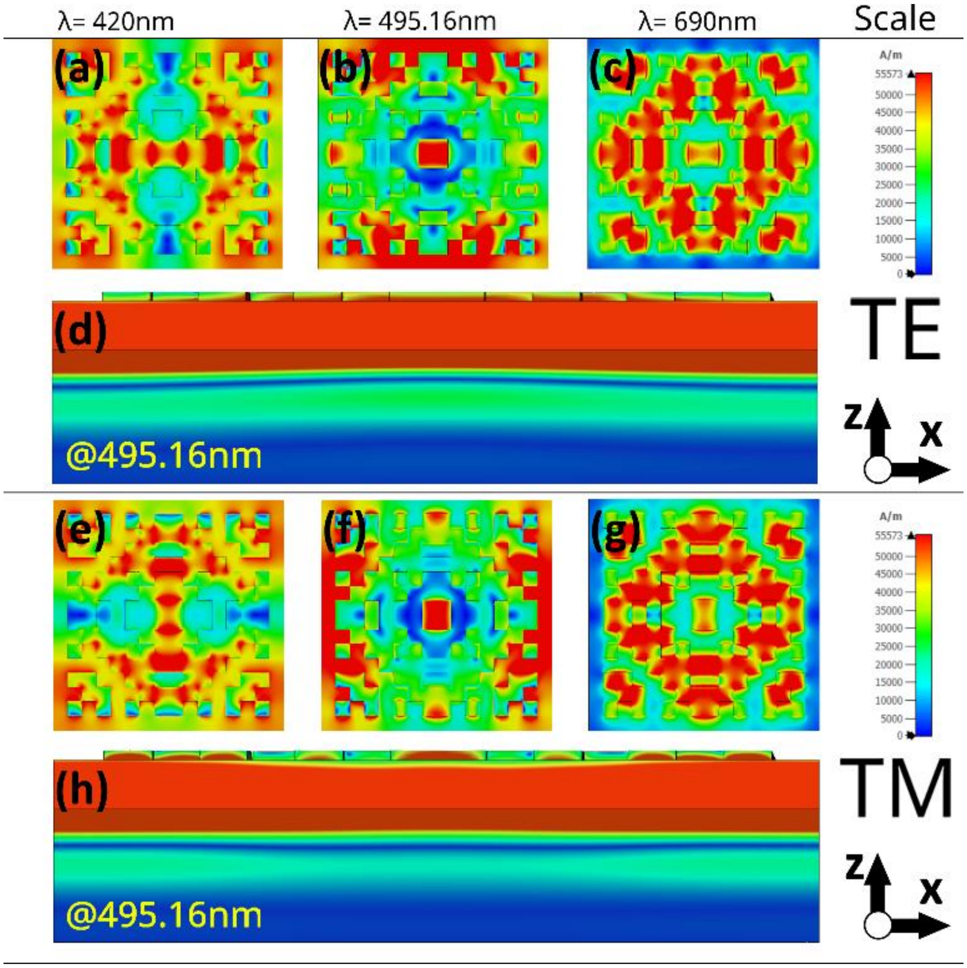

Fig. 7. Representation of magnetic-field distribution of the unit cell (a)-(c) for TE polarization in 420, 495.16, and 690 nm with linear color bar (Vm-1) in y-x axis, (d) cross-sectional view of the middle of the structure at 495.16nm (peak) resonance wavelength in z-x axis, (e)-(g) TM polarization in 420, 495.16, 690 nm with linear color bar (Vm-1) y-x axis, (h) cross-sectional view of the middle of the structure at 495.16nm (peak) resonance wavelength in z-x axis.

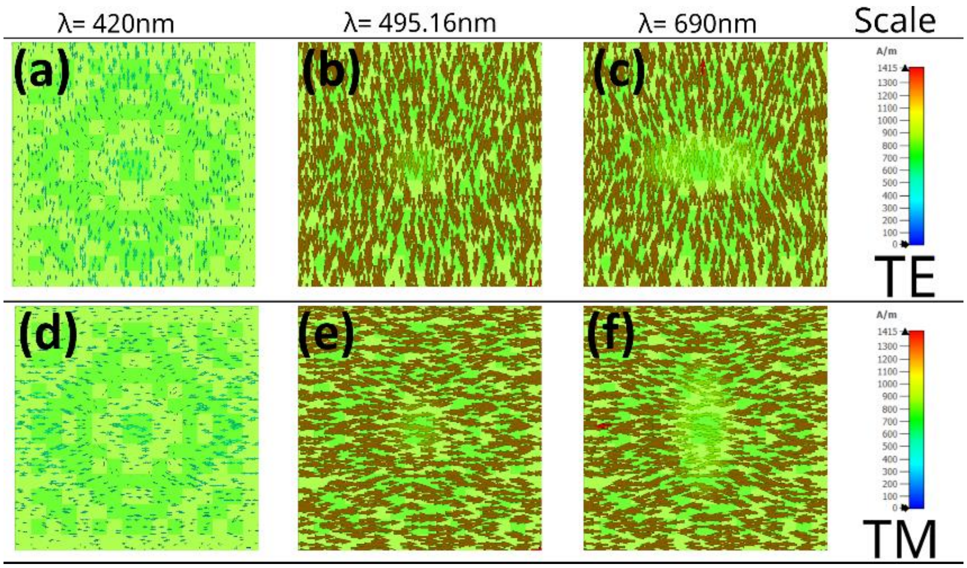

Fig. 8. Representation of cross-sectional view of surface charge distribution of the unit cell (a)-(c) for TE polarization in 420, 495.16, and 690 nm with linear color bar (Am-1) in y-x axis, (d)-(f) TE polarization in 420, 495.16, and 690 nm with linear color bar (Am-1) in y-x axis for normal incident angle. The cross section is done with an x-y axis.

3.6 Summary

Considering all aspects, our proposed solution is an optimal one. Here we showcased our different aspects of our HMMA from absorption, to theoretical verification. Also shown a comparison of different geometry and various dielectric substrate on the unit cell along with incident and polarization angle stability and electric, magnetic and surface current distribution.

CHAPTER 4

FUTURE WORK

4.1 Introduction

This chapter discusses the future scope or the implementation of this system. As our system is a simulation based, various forms of new features can be incorporated to this system as per the requirements.

4.2 Future Scope of Work

The main objective of developing this HMMA is for use case in solar power panels. But more to it due to restriction we were not able to verify our results experimentally, meaning an experimental output could be produced first. Afterward implementation in a STPV can be looked into to see verify the real life implications. It can also be implemented into optical sensors or light detectors, magnetic resonance imaging, plasmonic-sensors, and thermal imaging applications. Also looking into a use case of n-type SiO_2 could be considered.

4.3 Summary

This chapter has described the possible future applications of the design. But there are a lot of possibilities with the designed system. The system may need some research for different applications, though the principle of the designed system will remain as it is.

CHAPTER 5

RESULTS

5.1 Introduction

This chapter of the report contains the results that we achieved throughout the course of using this system.

5.2 Comparative study

Table 2 illustrates that our suggested HMMA might be extremely desired. After comparing our HMMA design to various previous studies with comparable characteristics and domains, it is clear that it outperforms other designs reported to date. In the end, our study demonstrated an ultra-thin MM absorber with very good temperature stability. It is also worth noting that the materials utilized in the production of our HMMA are less expensive than other materials like gold, silver, silicon, and so on. Our HMMA may also be scaled down to not just half the unit cell size, but a quarter unit cell size and still be effective as an optical absorber. The design is also highly functional at incident angles of up to 60°, which is important for energy harvesting and sensor applications. Another significant feature is that, since W is used as the base metal, it does not require the use of quartz or a glass layer, as other designs do. As a consequence of this feature, the cost of building this construction will be reduced. Because of its large bandwidth, high absorption peak of 99.99%, and the previously mentioned features, the suggested MM absorber is a powerful solution for many optical area applications.

Table 2. Comparison of the proposed unit cell's characteristics and bandwidth with that of prior studies.

Ref.#	Material	Layers	Peak Absorption	Polarization-insensitive & Angle ($A \geq 70\%$)	Absorption level	Validation
[24]	SiO_2-Au Composite, Glass, SiO_2, Au	Four	99%	Yes & $\theta \leq 60°$	Above 85%	Simulated & measured
[25]	Ai & Kerr	Four	99%	Yes & $\theta \leq 40°$	Above 80%	Simulated
[26]	Ni & Si	Three	99%	Yes & $\theta \leq 60°$	Above 90%	Simulated & measured
[27]	Au & SiO_2	Three	99%	Yes & $\theta \leq 40°$	Above 90%	Simulated & optimized
[28]	Ni	Two	99.8%	Yes & $\theta \leq 60°$	Above 85%	Simulated & measured
[29]	W & SiO_2	Three	99.99%	Yes & $\theta \leq 60°$	Above 91.6%	Simulated & calculated
[30]	W & SiO_2	Three	99.99%	Yes & $\theta \leq 60°$	Above 91.24%	Simulated & calculated
[31]	W & Quartz	Three	99.92%	Yes & $\theta \leq 45°$	Above 66.66%	Simulated
[32]	Au & SiO_2	Three	99.9%	Yes & $\theta \leq 80°$	Above 40%	Simulated & measured
[33]	W & SiO_2	Three	99%	Yes & $\theta \leq 30°$	Above 85%	Simulated
[Proposed]	W & SiO_2	Three	99.99%	Yes & $\theta \leq 70°$	Above 91.4%	Simulated & calculated

5.3 Summary

This chapter has covered the different types of results that we have managed to obtain throughout the course of using this system.

CHAPTER 6

CONCLUSION

Conclusion: We constructed and theoretically validated a novel three-layer broadband, polarization independent, ultra-thin MM absorber consisting of Wand SiO2, with a metasurface structure based on Hadamard-matrix and a metasurface structure based on Hadamard-matrix. As a result of the experiments, we discovered that our HMMA displays good absorption across a wide spectrum spanning the optical domain in both the TE and TM modes, with a peak value of 99.99% for both modes. Furthermore, with an average absorption of 97.15%, it is very effective. Because of the strong demand in the optical sector and the simplicity of the geometry, the proposed design might be used for light detectors, a true invisibility cloak, optical sensors, magnetic resonance imaging, plasmonic sensors, and other high thermal imaging applications.

BIBLIOGRAPHY

1. V. G. Veselago, "The Electrodynamic of Substances with Simultaneous Negative Values of e and μ," Sov. Phys. Uspekhi **10**, 509–514 (1968).

2. N. I. Zheludev, "The road ahead for metamaterials," Science (80-.). **328**, 582–583 (2010).

3. Y. Liu and X. Zhang, "Metamaterials: A new frontier of science and technology," Chem. Soc. Rev. **40**, 2494–2507 (2011).

4. M. Silveirinha and N. Engheta, "Tunneling of electromagnetic energy through subwavelength channels and bends using ε-near-zero materials," Phys. Rev. Lett. **97**, (2006).

5. J. B. Pendry, "Negative refraction makes a perfect lens," Phys. Rev. Lett. **85**, 3966–3969 (2000).

6. D. R. Smith, W. J. Padilla, D. C. Vier, S. C. Nemat-Nasser, and S. Schultz, *Composite Medium with Simultaneously Negative Permeability and Permittivity* (2000).

7. S. H. Lee, C. M. Park, Y. M. Seo, and C. K. Kim, "Reversed Doppler effect in double negative metamaterials," Phys. Rev. B - Condens. Matter Mater. Phys. **81**, 1–4 (2010).

8. Z. Duan, X. Tang, Z. Wang, Y. Zhang, X. Chen, M. Chen, and Y. Gong, "Observation of the reversed Cherenkov radiation," Nat. Commun. **8**, 1–7 (2017).

9. W. Cai and V. Shalaev, *Optical Metamaterials: Fundamentals and Applications* (Springer New York, 2010).

10. Y. Huang, Y. Feng, and T. Jiang, "Electromagnetic cloaking by layered structure of homogeneous isotropic materials," Opt. Express **15**, 11133 (2007).

11. A. Sarsen and C. Valagiannopoulos, "Robust polarization twist by pairs of multilayers with tilted optical axes," Phys. Rev. B **99**, 1–10 (2019).

12. D. Rodrigo, O. Limaj, D. Janner, D. Etezadi, F. J. G. De Abajo, V. Pruneri, and H. Altug, "Rodrigo2015.Pdf," (2015).

13. F. Ding, Y. Cui, X. Ge, Y. Jin, and S. He, "Ultra-broadband microwave metamaterial

absorber," Appl. Phys. Lett. **100**, 2010–2014 (2012).

14. S. H. Raad and Z. Atlasbaf, "Tunable optical meta-surface using graphene-coated spherical nanoparticles," AIP Adv. **9**, (2019).

15. M. A. Baqir and P. K. Choudhury, "Hyperbolic Metamaterial-Based UV Absorber," IEEE Photonics Technol. Lett. **29**, 1548–1551 (2017).

16. M. A. Baqir and P. K. Choudhury, "On the VO 2 metasurface-based temperature sensor," JOSA B **36**, F123--F130 (2019).

17. R. M. H. Bilal, M. A. Saeed, P. K. Choudhury, M. A. Baqir, W. Kamal, M. M. Ali, and A. A. Rahim, "Elliptical metallic rings-shaped fractal metamaterial absorber in the visible regime," Sci. Rep. **10**, 1–12 (2020).

18. S. Mahmud, M. Karim, S. S. Islam, M. M. K. Shuvo, T. Akter, A. F. Almutairi, and M. T. Islam, "A Multi-Band Near Perfect Polarization and Angular Insensitive Metamaterial Absorber with a Simple Octagonal Resonator for Visible Wavelength," IEEE Access **9**, 117746–117760 (2021).

19. S. Hossain, M. I. H. Patwary, S. S. Islam, S. Mahmud, N. B. Misran, A. F. Almutairi, and M. T. Islam, "Double-E-Triple-H-Shaped NRI-Metamaterial for Dual-Band Microwave Sensing Applications," Comput. Mater. Contin. **71**, 5817–5836 (2022).

20. N. I. Landy, S. Sajuyigbe, J. J. Mock, D. R. Smith, and W. J. Padilla, "Perfect metamaterial absorber," Phys. Rev. Lett. **100**, 1–4 (2008).

21. S. Ju, S. H. A. Shah, M. A. Javed, J. Li, G. Palteru, J. Robin, Y. Xing, O. Kanhere, and T. S. Rappaport, "Scattering Mechanisms and Modeling for Terahertz Wireless Communications," IEEE Int. Conf. Commun. **2019-May**, 1–7 (2019).

22. M. TONOUCHI, "Cutting-edge terahertz technology," Nat. Photonics **1**, 97–105 (2002).

23. Y. P. Lee, P. V. Tuong, H. Y. Zheng, J. Y. Rhee, and W. H. Jang, "An application of metamaterials: Perfect absorbers," J. Korean Phys. Soc. **60**, 1203–1206 (2012).

24. M. K. Hedayati, M. Javaherirahim, B. Mozooni, R. Abdelaziz, A. Tavassolizadeh, V. S.

K. Chakravadhanula, V. Zaporojtchenko, T. Strunkus, F. Faupel, and M. Elbahri, "Design of a perfect black absorber at visible frequencies using plasmonic metamaterials," Adv. Mater. **23**, 5410–5414 (2011).

25. X. Duan, S. Chen, W. Liu, H. Cheng, Z. Li, and J. Tian, "Polarization-insensitive and wide-angle broadband nearly perfect absorber by tunable planar metamaterials in the visible regime," J. Opt. (United Kingdom) **16**, 125107 (2014).

26. M. LUO, S. SHEN, L. ZHOU, S. WU, Y. ZHOU, and L. CHEN, "Broadband, wide-angle, and polarization- independent metamaterial absorber for the visible regime," Opt. Express **25**, 16715–16724 (2017).

27. M. H. Heidari and S. H. Sedighy, "Broadband wide-angle polarization-insensitive metasurface solar absorber," J. Opt. Soc. Am. A **35**, 522 (2018).

28. Y. Zhou, M. Luo, S. Shen, H. Zhang, D. Pu, and L. Chen, "Cost-effective near-perfect absorber at visible frequency based on homogenous meta-surface nickel with two-dimension cylinder array," Opt. Express **26**, 27482 (2018).

29. S. Mahmud, S. S. Islam, A. F. Almutairi, and M. T. Islam, "A Wide Incident Angle, Ultrathin, Polarization-Insensitive Metamaterial Absorber for Optical Wavelength Applications," IEEE Access **8**, 129525–129541 (2020).

30. S. Mahmud, S. S. Islam, K. Mat, M. E. H. Chowdhury, H. Rmili, and M. T. Islam, "Design and parametric analysis of a wide-angle polarization-insensitive metamaterial absorber with a star shape resonator for optical wavelength applications," Results Phys. **18**, 103259 (2020).

31. I. Hossain, M. Samsuzzaman, M. Moniruzzaman, B. B. Bais, M. S. J. Singh, and M. T. Islam, "Polarization-Independent Broadband Optical Regime Metamaterial Absorber for Solar Harvesting: A Numerical Approach," Chinese J. Phys. **71**, 699–715 (2021).

32. Y. Zhang, Z. Yi, X. Wang, P. Chu, W. Yao, Z. Zhou, S. Cheng, Z. Liu, P. Wu, M. Pan, and Y. Yi, "Dual band visible metamaterial absorbers based on four identical ring patches," Phys. E Low-dimensional Syst. Nanostructures **127**, 114526 (2021).

33. S. Charola, S. K. Patel, K. Dalsaniya, R. Jadeja, T. K. Nguyen, and V. Dhasarathan, "Numerical investigation of wideband L-shaped metasurface based solar absorber for visible and ultraviolet region," Phys. B Condens. Matter **601**, 412503 (2021).

34. G. Ghosh, "Dispersion-equation coefficients for the refractive index and birefringence of calcite and quartz crystals," Opt. Commun. **163**, 95–102 (1999).

35. P. M. Schneidert and W. B. Fowler, "Band Structure and Optical Properties of Silicon Dioxide," Phys. Rev. Lett. **36**, 8–11 (1976).

36. R. K. Yarlagadda and J. E. Hershey, *Hadamard Matrix Analysis and Synthesis: With Applications to Communications and Signal/Image Processing* (2012).

37. E. J. Rothwell, J. L. Frasch, S. M. Ellison, P. Chahal, and R. O. Ouedraogo, "Analysis of the Nicolson-Ross-Weir method for characterizing the electromagnetic properties of engineered materials," Prog. Electromagn. Res. **157**, 31–47 (2016).

38. T. Wanghuang, W. Chen, Y. Huang, and G. Wen, "Analysis of metamaterial absorber in normal and oblique incidence by using interference theory," AIP Adv. **3**, 0–9 (2013).

39. H.-T. Chen, "Interference theory of metamaterial perfect absorbers," Opt. Express **20**, 7165 (2012).

40. H. T. Chen, J. Zhou, J. F. O’Hara, F. Chen, A. K. Azad, and A. J. Taylor, "Antireflection coating using metamaterials and identification of its mechanism," Phys. Rev. Lett. **105**, 1–4 (2010).

41. D. R. Smith, D. C. Vier, T. Koschny, and C. M. Soukoulis, "Electromagnetic parameter retrieval from inhomogeneous metamaterials," Phys. Rev. E - Stat. Nonlinear, Soft Matter Phys. **71**, 1–11 (2005).

42. X. Han, K. He, Z. He, and Z. Zhang, "Tungsten-based highly selective solar absorber using simple nanodisk array," Opt. Express **25**, A1072 (2017).

43. H. M. Lee and J. C. Wu, "A wide-angle dual-band infrared perfect absorber based on metaldielectricmetal split square-ring and square array," J. Phys. D. Appl. Phys. **45**, (2012).

44. S. Lee, T. Q. Tran, H. Heo, M. Kim, and S. Kim, "A proposal of a perfect graphene absorber with enhanced design and fabrication tolerance," Sci. Rep. **7**, 1–10 (2017).

45. T. Cao, L. Zhang, R. E. Simpson, and M. J. Cryan, "Mid-infrared tunable polarization-independent perfect absorber using a phase-change metamaterial," JOSA B **30**, 1580–1585 (2013).

APPENDIX

SOFTWARE LISTING

About Programs

All simulations was done in CST Microwave Studio.

<attached to disk>

Data manipulation using MATLAB and C++

```
clc;
clf;
clear all;

s11=readtable('s11.csv');
s12=readtable('s12.csv');
rx=dlmread('s11.csv',',',1,0);
tx=dlmread('s12.csv',',',1,0);
s11=dlmread('s11.csv',',',1,0);
[a]=s11(:,3)*-1;
s11=(s11(:,1:2));
s11=[s11,a];

s12=dlmread('s12.csv',',',1,0);
[b]=s12(:,3)*-1;
s12=(s12(:,1:2));
s12=[s12,b];

f=s11(:,1)*1e12;
c=3e8;
k=(2*pi/3e8)*f;
d=5.5e-8;

rx=s11;
tx=s12;


s11=s11(:,2).*(cos(s11(:,3))+i*sin(s11(:,3)));
s12=s12(:,2).*(cos(s12(:,3))+i*sin(s12(:,3)));

z=((((1+s11).^2)-s12.^2)./(((1-s11).^2)-s12.^2)).^0.5;
tmp=(z-1)./(z+1);
exp=s12./(1-s11.*tmp);
y=(imag(log(exp))-i.*real(log(exp)));
m=k*d;
n=(imag(log(exp))-i.*real(log(exp)))./(k*d);
```

```
%n=((log(exp))-i.*(log(exp)))./(k*d);
eps_eff=n./z;
mu_eff=n.*z;

%plot the curves
figure
subplot(2,2,1)

plot(rx(:,1),real(mu_eff),'--k',rx(:,1),imag(mu_eff),'k');
grid ON;
legend('Re(\mu_e_f_f)','imag(\mu_e_f_f)')
xlabel('freq(THZ)');
ylabel('real and imag permeability');

subplot(2,2,2)
plot(rx(:,1),real(eps_eff),'--k',rx(:,1),imag(eps_eff),'k')
grid ON;
legend('Re(\epsilon_e_f_f)','imag (\epsilon_e_f_f)')
xlabel('freq(THZ)');
ylabel('real and imag permittivity');

subplot(2,2,3)
plot(rx(:,1),real(n),'--k',rx(:,1),imag(n),'k')
grid ON;
legend('Re(n)','Imag(n)')
xlabel('freq(THZ)');
ylabel('real and Imag  refractive index ');

subplot(2,2,4)
plot(rx(:,1),real(z),'--k',rx(:,1),imag(z),'k')
grid ON;
legend('Re(z)','Imag(z)')
xlabel('freq(THZ)');
ylabel('real and imag impedance');

addpath(genpath('API PATH HERE'));

cst = actxserver('CSTStudio.application');
mws = cst.invoke('NewMWS');

Geometry = 'nm';
Frequency = 'THz';
Time = 'ns';
TemperatureUnit = 'Kelvin';
Voltage = 'V';
Current = 'A';
```

```
Resistance = 'Ohm';
Conductance  = 'S';
Capacitance = 'PikoF';
Inductance = 'NanoH';

CstDefineUnits(mws,Geometry, Frequency, Time, TemperatureUnit, Voltage, Current,
Resistance, Conductance, Capacitance, Inductance)
ComponentList = 'component1';
CstDefineFrequencyRange(mws,0.5,10)
CstMeshInitiator(mws)

% Defining the boundary conditions. We need to simulate a plane wave here so we need a
waveguide-like
% structure therefore the 'walls' of the structure need to be perfect
% electric and perfect magnetic according to the orientation of our
% electromagnetic field
minfrequency = 0.5;
Xmin = 'electric';
Xmax = 'electric';
Ymin = 'magnetic';
Ymax = 'magnetic';
Zmin = 'open(add space)';
Zmax = 'open (add space)';
CstDefineOpenBoundary(mws,minfrequency,Xmin,Xmax,Ymin,Ymax,Zmin,Zmax)

XminSpace = 0;
XmaxSpace = 0;
YminSpace = 0;
YmaxSpace = 0;
ZminSpace = 0;
ZmaxSpace = 0;
CstDefineBackroundMaterial(mws,XminSpace,XmaxSpace, YminSpace, YmaxSpace,
ZminSpace, ZmaxSpace)

CstTungsten(optical)(mws)
CstSilicondioxide(optical)(mws)

Name = 'Substrate';
component = 'component1';
material = 'Silicondioxide';
Xrange = [0 480];
Yrange = [0 480];
Zrange = [0 55];
Cstbrick(mws, Name, component, material, Xrange, Yrange, Zrange)

% making the copper wire at the bottom of the substrate
```

```
Name = 'Backconductor';
component = 'component1';
material = ‘Tungsten (optical)';
Xrange = [0 480];
Yrange = [0 480];
Zrange = [-150 0];
Cstbrick(mws, Name, component, material, Xrange, Yrange, Zrange)

% Making the front design
%Assigning different squares to make the design
%<rest in disk>

%Assigning the ports
PortNumber = 1;
Xrange = [0 0];
Yrange = [0 0];
Zrange = [1 -1];
XrangeAdd = [0 0];
YrangeAdd = [0 0];
ZrangeAdd = [1 -1];
CstWaveguidePort(mws,PortNumber, Xrange, Yrange, Zrange, XrangeAdd, YrangeAdd,
ZrangeAdd, 'Full','xmin')

PortNumber = 2;
Xrange = [0 0];
Yrange = [0 0];
Zrange = [1 1];
XrangeAdd = [0 0];
YrangeAdd = [0 0];
ZrangeAdd = [1 1];
CstWaveguidePort(mws,PortNumber, Xrange, Yrange, Zrange, XrangeAdd, YrangeAdd,
ZrangeAdd, 'Full','xmax')

CstSaveProject(mws)
CstDefineTimedomainSolver(mws,-40)
```